Eur. Phys. J. A **21**, 335–348 (2004)
DOI 10.1140/epja/i2004-10001-5

THE EUROPEAN PHYSICAL JOURNAL A

Electron scattering on ^{3}He —A playground to test nuclear dynamics

W. Glöckle[1,a], J. Golak[2], R. Skibiński[2], H. Witała[2], H. Kamada[3], and A. Nogga[4]

[1] Institut für Theoretische Physik II, Ruhr Universität Bochum, D-44780 Bochum, Germany
[2] M. Smoluchowski Institute of Physics, Jagiellonian University, PL-30059 Kraków, Poland
[3] Department of Physics, Faculty of Engineering, Kyushu Institute of Technology, 1-1 Sensuicho, Tobata, Kitakyushu 804-8550, Japan
[4] Institute for Nuclear Theory, University of Washington, Seattle, WA 98195-1550, USA

Received: 6 February 2004 /
Published online: 17 August 2004 –
Communicated by U.-G. Meißner

Abstract. The electron-induced processes on ^{3}He are analyzed using the Faddeev formalism with modern nucleon-nucleon and three-nucleon forces as well as exchange currents. The kinematical region is restricted to a mostly nonrelativistic one where the three-nucleon c.m. energy is below the pion production threshold and the three-momentum of the virtual photon is sufficiently below the nucleon mass. Comparisons with available data are shown and cases of agreement and disagreement are found. It is argued that new and precise data are needed to systematically check the present-day dynamical ingredients.

PACS. 21.45.+v Few-body systems – 21.10.-k Properties of nuclei; nuclear energy levels – 25.10.+s Nuclear reactions involving few-nucleon systems – 25.20.-x Photonuclear reactions

1 Introduction

If one chooses energy and momenta of the virtual photon so that the three-nucleon (3N) c.m. energy in the final state is below the pion production threshold and the total 3N momentum in the lab system remains sufficiently well below the nucleon mass, a nonrelativistic approach is generally well justified. In that kinematical region nucleon-nucleon (NN) forces are well tuned and the 2N data are described with high precision. Also 3N forces are adjusted to the binding energy of the ^{3}H nucleus. In principle the interplay of those two types of dynamical ingredients can and should be tested via the rich set of 3N scattering observables. A successful test would guarantee a correct description of the final-state interaction for electron-induced inelastic processes on ^{3}He. It would also provide confidence that the ^{3}He bound-state wave function is reliable. Those tests are still going on using nucleon-deuteron (Nd) elastic scattering and breakup reactions. Though overall one can say already now [1] that the great bulk of the existing 3N scattering data is quite well described by the present-day force models, the situation, however, is by far not ideal because the 3N force properties are still rather unsettled [2]. If the ideal situation of a successful description of 3N scattering observables was reached, the only new dynamical ingredient in electron scattering on ^{3}He would be the electromagnetic nucleonic current operator. Nowadays, this still poses a serious challenge, because a general, sound parametrization has not been found yet. In such a situation combined efforts, in the pure 3N sector and in electron-induced processes, appear advisable to progress. This needs a solid ground of data.

In this paper we would like to exemplify that electron-induced processes on ^{3}He (without/with polarized electron beam and/or without/with polarized ^{3}He target) provide a very rich playground to test nuclear dynamics. We show that their description requires the full list of dynamical ingredients. We will see that the results of an often used approximation in which the photon is absorbed by just one nucleon and the two spectator nucleons interact in first order in the NN t-operator (this corresponds to the standard approximation leading to the widely used concept of the spectral function) are by far not sufficient and the final-state interaction among all three nucleons is essential. In addition, in many configurations, absorption of the photon by two-nucleon currents is important and even effects of 3N forces are visible. The presented examples will clearly illustrate that there are

[a] e-mail: walterg@tp2.ruhr-uni-bochum.de

observables for electron scattering on ^{3}He, which reflect the various dynamical ingredients in a sensitive manner. The results would be very unreliable if simple-minded approximations in the analysis were used.

In sect. 2 we briefly review our theoretical framework. Then, in sect. 3, we display various observables for electron-induced processes on ^{3}He which show both agreement and disagreement with theory. The need for additional data is pointed out to challenge the present-day theory in a more specific and systematic manner than it has been done up to now. We end with an outlook in sect. 4.

2 Theoretical framework

The central quantities in the description of electron-induced processes are the nuclear matrix elements:

$$N^\mu \equiv \left\langle \Psi_f^{(-)} \mid j^\mu(\vec{Q}) \mid \Psi_{^3\mathrm{He}}^{\theta^*\phi^*} \right\rangle . \tag{1}$$

They are composed of the polarized ^{3}He target state, the components $j_\mu(\vec{Q})$ of the current operator and the final 3N scattering state $\langle \Psi_f^{(-)} \mid$ with asymptotic momenta and spin quantum numbers f. For proton-deuteron (pd) breakup these are the proton and deuteron momenta and their spin magnetic quantum numbers, and for the full breakup the three-final-nucleon momenta and again their spin magnetic quantum numbers. In the latter case one has to add the isospin labels. The initial ^{3}He spin direction is determined by the angle θ^* with respect to the photon momentum $\vec{Q}$ and by the azimuthal angle ϕ^* in relation to the scattering plane formed by the initial- and final-electron momenta.

The ^{3}He state is a solution [3] of the Faddeev equation

$$\psi = G_0 t P \psi + G_0(1 + tG_0)V_4^{(1)}(1 + P)\psi, \tag{2}$$

where the Faddeev component ψ determines the full state via

$$\Psi_{^3\mathrm{He}} = (1 + P)\psi. \tag{3}$$

The ingredients are the free 3N propagator G_0, the NN t-operator generated via the Lippmann-Schwinger equation from any modern NN interaction and a suitably chosen permutation operator P [4]. Further $V_4^{(1)}$ is one of the three parts of a 3N force into which any 3NF can be decomposed. We assume here that the t-operator acts in the pair 23 and that $V_4^{(1)}$ is the part of the three-nucleon force which is symmetrical under exchange of particles 2 and 3.

It is advisable not to evaluate the scattering states separately but to redirect the action of the Möller wave operator towards the current and the target state. This leads [5] to the following form of the nuclear matrix element:

$$N^\mu = \langle \psi_f \mid U^\mu \rangle, \tag{4}$$

where the auxiliary state $\mid U^\mu \rangle$ obeys the Faddeev-like integral equation

$$\begin{aligned} \mid U^\mu \rangle &= (1 + P) j^\mu(\vec{Q}) \mid \Psi_{^3\mathrm{He}} \rangle \\ &\quad + PtG_0 \mid U^\mu \rangle + (1 + P)V_4^{(1)} G_0(tG_0 + 1) \mid U^\mu \rangle. \end{aligned} \tag{5}$$

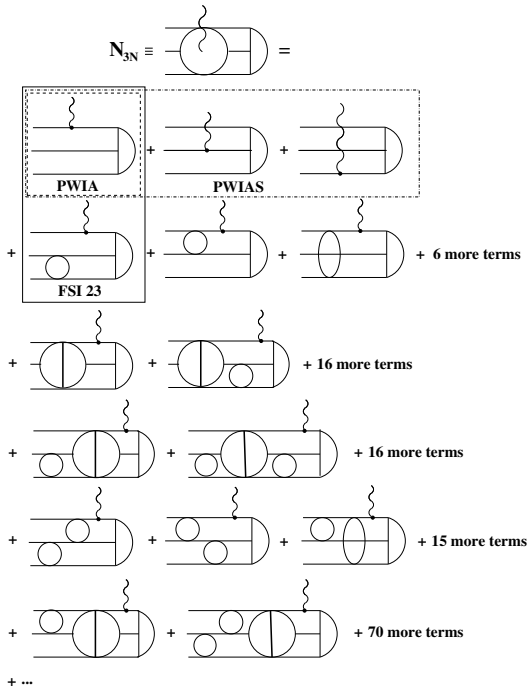

Fig. 1. Diagrammatic representation of the nuclear matrix element for the three-body electrodisintegration of ^{3}He. The open circles and ovals represent the two-body t-matrices. The big circles with a vertical line denote the action of $V_4^{(1)}$. Three horizontal lines between photon absorption and forces, and between forces describe free propagation. The half-moon symbol on the very right stands for ^{3}He.

$|\psi_f\rangle$ is a known channel-dependent state, which for the pd case is just the deuteron state together with a plane wave for the third particle, $|\psi_f^{\mathrm{pd}}\rangle = |\phi_{\mathrm{d}}\vec{q}\rangle$. For the complete three-body breakup it is given as $|\psi_f^{\mathrm{3N}}\rangle = (1 + G_0 t)|\phi_0\rangle$, with $|\phi_0\rangle$ being plane waves, antisymmetrized in the two-body subsystem, where t acts.

We see in eq. (5) a similar type of Faddeev-like equation as for the bound state, but now there are singularities in t and G_0, which have to be treated appropriately. This equation is not suitable for numerical applications (except for forces of finite rank) because the permutation operator stands to the very left [6]. The equation can be rewritten to an appropriate form suitable for numerical implementation [5]. In order to display the physical content of the matrix element it is, however, quite adequate. To that aim we iterate eq. (5). In obvious notation it reads

$$\mid U^\mu \rangle = \mid U_0^\mu \rangle + K_{\mathrm{NN}} \mid U^\mu \rangle + K_{\mathrm{3N}} \mid U^\mu \rangle \tag{6}$$

and after iteration

$$\begin{aligned} \mid U^\mu \rangle &= \mid U_0^\mu \rangle + (K_{\mathrm{NN}} + K_{\mathrm{3N}}) \mid U_0^\mu \rangle \\ &\quad + (K_{\mathrm{NN}} + K_{\mathrm{3N}})(K_{\mathrm{NN}} + K_{\mathrm{3N}}) \mid U_0^\mu \rangle + \cdots . \end{aligned} \tag{7}$$

The resulting terms building up N^μ are depicted in fig. 1 for the case of complete breakup.

In general the series shown in fig. 1 converges very slowly or even diverges [7,8]. Therefore it is important to

rely on the full solution of eq. (5), which also guarantees that $\langle \Psi_f^{(-)} \mid$ and $\mid \Psi_{^3\mathrm{He}} \rangle$ are consistent solutions to the same 3N Hamiltonian.

For the current operator we use the standard nonrelativistic single-nucleon piece and two-body currents of the π- and ρ- exchange type related to the AV18 NN force [9] as proposed by Riska [10]. In case of elastic electron scattering on ^{3}He the charge form factor is known [11] to be sensitive to an additional two-body density operator and we use the seagull terms from [12].

The formulation just presented is applicable for all sorts of inelastic electron-induced processes on ^{3}He. In case of inclusive processes one can also use an alternative approach which is based on the closure relation. The generic form for a response function in inclusive processes is

$$\begin{aligned} R(\omega) &= \sum_f \left| \langle \Psi_f^{(-)} \mid \hat{O} \mid \Psi_i \rangle \right|^2 \delta(\omega + E_i - E_f) \\ &= \sum_f \langle \Psi_i \mid \hat{O}^\dagger \mid \Psi_f^{(-)} \rangle \delta(\omega + E_i - E_f) \langle \Psi_f^{(-)} \mid \hat{O} \mid \Psi_i \rangle \\ &= \sum_f \langle \Psi_i \mid \hat{O}^\dagger \delta(\omega + E_i - H) \mid \Psi_f^{(-)} \rangle \langle \Psi_f^{(-)} \mid \hat{O} \mid \Psi_i \rangle \\ &= \langle \Psi_i \mid \hat{O}^\dagger \delta(\omega + E_i - H) \hat{O} \mid \Psi_i \rangle \\ &= -\frac{1}{\pi} \Im \left(\langle \Psi_i \mid \hat{O}^\dagger \frac{1}{E + i\epsilon - H} \hat{O} \mid \Psi_i \rangle \right), \end{aligned} \tag{8}$$

where E is now the internal c.m. 3N energy. This suggests to define an auxiliary state

$$\mid \Psi_{\hat{O}} \rangle \equiv \frac{1}{E + i\epsilon - H} \hat{O} \mid \Psi_i \rangle. \tag{9}$$

That auxiliary state $\mid \Psi_{\hat{O}} \rangle$ fulfills an inhomogeneous Schrödinger equation

$$(H - E) \mid \Psi_{\hat{O}} \rangle = \hat{O} \mid \Psi_i \rangle, \tag{10}$$

which can again be solved precisely by a Faddeev-like formulation. It results in

$$\mid \Psi_{\hat{O}} \rangle = G_0 (1 + P) U, \tag{11}$$

where U obeys

$$\begin{aligned} U = (1 + tG_0) O^{(1)} \mid \Psi_i \rangle + tG_0 P U \\ + (1 + tG_0) V_4^{(1)} G_0 (1 + P) U \end{aligned} \tag{12}$$

and the operator $\hat{O}$ has been decomposed as $\hat{O} = O^{(1)} + O^{(2)} + O^{(3)}$, which is always possible. We refer to [7] and to [13] where also the slightly more intricate case with polarized particles is described. Again we would like to graphically illustrate the physical content, now for the final expression of eq. (8). Iterating the Faddeev-like equation (12) for the quantity U one obtains the series of processes depicted in fig. 2.

Our numerical accuracy in the observables is of the order of one percent. It should also be noticed that all

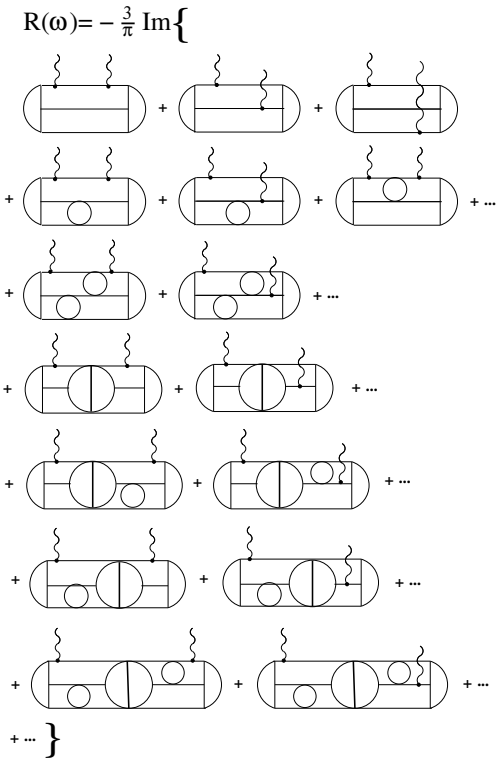

Fig. 2. The processes contributing to the inclusive response function $R(\omega)$ from eq. (8), where $\hat{O}$ is photon absorption on a single nucleon. Symbols are as in fig. 1.

dynamical ingredients are fixed and no free parameters are used (except in the case that the neutron form factors are determined). If not otherwise stated we always use in this paper the AV18 NN force, the Urbana IX 3NF [14] and the currents as mentioned above.

Usually the vector part of N^μ is decomposed into a component parallel to the photon momentum $\vec{Q}$ and one transversal to it, where the parallel component is eliminated with the help of the continuity equation in favor of the density matrix element N^0. This leads to the standard expressions for the cross-sections [15,16] in terms of response functions R_i, the analytically known kinematical factors v_i, and the electron beam helicity h:

$$\begin{aligned} \mathrm{d}\sigma = \sigma_{\mathrm{Mott}} \frac{1}{(E_{\mathrm{e}'})^2} \delta^4(P_f - P_i - Q)\, \mathrm{d}^3k_{\mathrm{e}'}\, \mathrm{d}^3p_1\, \mathrm{d}^3p_2\, \mathrm{d}^3p_3 \\ \times \Big[v_L R_L + v_T R_T + v_{TT} R_{TT} + v_{TL} R_{TL} \\ + h \left(v_{TL'} R_{TL'} + v_{T'} R_{T'} \right) \Big]. \end{aligned} \tag{13}$$

Thus the eightfold differential cross-section $\mathrm{d}^8\sigma / (\mathrm{d}E_{\mathrm{e}'} \mathrm{d}\Omega_{\mathrm{e}'} \mathrm{d}\Omega_1 \mathrm{d}\Omega_2 \mathrm{d}E_1)$ for complete breakup reads

$$\begin{aligned} \frac{\mathrm{d}^8\sigma}{\mathrm{d}E_{\mathrm{e}'} \mathrm{d}\Omega_{\mathrm{e}'} \mathrm{d}\Omega_1 \mathrm{d}\Omega_2 \mathrm{d}E_1} = \\ \sigma_{\mathrm{Mott}} \left[v_L R_L + v_T R_T + v_{TT} R_{TT} + v_{TL} R_{TL} \right. \\ \left. + h \left(v_{TL'} R_{TL'} + v_{T'} R_{T'} \right) \right] \rho_f, \end{aligned} \tag{14}$$

where the phase space factor ρ_f in terms of final-nucleon laboratory momenta $\vec{p}_i$ and the nucleon mass m is

$$\rho_f = \frac{m p_1 p_2^2}{\left| \frac{p_2}{m} - \frac{\vec{p}_2 \cdot \vec{p}_3}{m p_2} \right|}. \tag{15}$$

Note that the matrix elements which appear in R_i in eqs. (13) and (14) are calculated for a polarized initial ^{3}He state. If the final polarizations are not measured, we sum the response functions over the magnetic quantum numbers of the three final nucleons. In particular,

$$R_L \equiv \sum_{m_1,m_2,m_3} \left| N^0(\vec{p}_1,\vec{p}_2,\vec{p}_3;m_1,m_2,m_3;\nu_1,\nu_2,\nu_3;\theta^*,\phi^*) \right|^2, \tag{16}$$

where m_1, m_2, m_3 are spin magnetic quantum numbers, and ν_1, ν_2, ν_3 are isospin magnetic quantum numbers needed to identify the nucleons in the final state.

3 Selected observables

In the following subsections we will present the various types of observables. Some of them have been presented before in [17] based on less complete dynamical ingredients. As emphasized in the introduction the kinematics is restricted such that a nonrelativistic treatment appears justified.

3.1 Elastic electron scattering

Figures 3 and 4 display the charge and magnetic form factors in elastic electron scattering on ^{3}He and ^{3}H, respectively. The agreement with the data for the lower q-values is reasonable but requires two-body densities for the charge form factors and two-body currents for the magnetic form factors. The discrepancies at the higher q-values ($q \geq 3$ fm^{-1}) clearly show that relativistic effects have to be taken seriously into account at such large momenta.

3.2 Inclusive electron scattering

The response functions R_L and R_T are displayed in figs. 5 and 6 for Q = 300, 400, 500, and 600 MeV/c. The double-dashed line is the non-symmetrized plane-wave result (PWIA), where the absorption of the photon takes place on just one nucleon by a single-nucleon current (see fig. 1.) Later on we also use symmetrized plane wave (PWIAS), where the photon is absorbed on all three nucleons by a single-nucleon current operator but all final-state interactions are still neglected. In the approximate treatment of FSI, called FSI23 for short, only interactions of the nucleons, which did not absorb the photon, are taken into account. For this case, the nuclear matrix element is not antisymmetrized in the final state (which mathematically

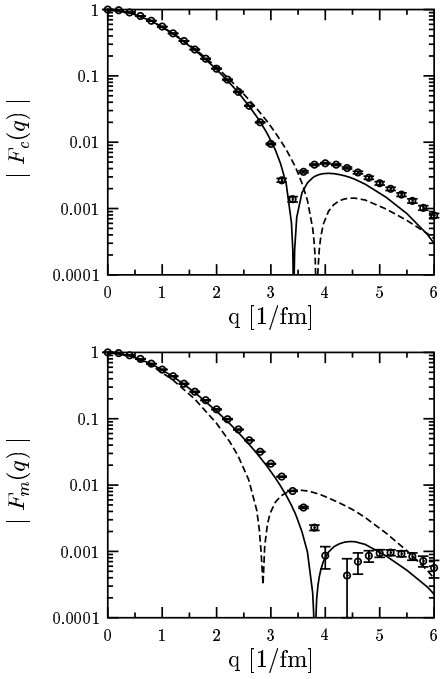

Fig. 3. The elastic charge ($|F_c(q)|$) and magnetic ($|F_m(q)|$) form factors of ^{3}He. The dashed lines correspond to the single-nucleon current calculations. The results including MEC (and in the case of the charge form factor also the $(p/m)^2$ corrections) are shown with the solid lines. The data are from [18].

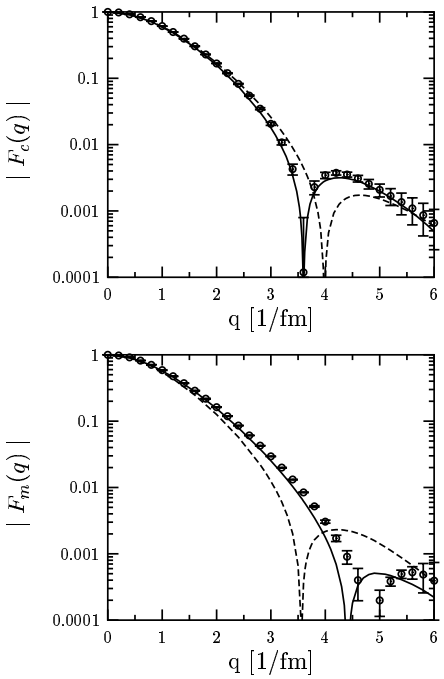

Fig. 4. The same as in fig. 3 for ^{3}H.

is identical to the assumption that the photon is absorbed only on one of the three nucleons, not in a symmetrized manner on all three). FSI stands for the complete calculation with all final-state interactions (exact 3N scattering state $\langle \Psi_f^{(-)}|$). The further curves for R_L in fig. 5 allow

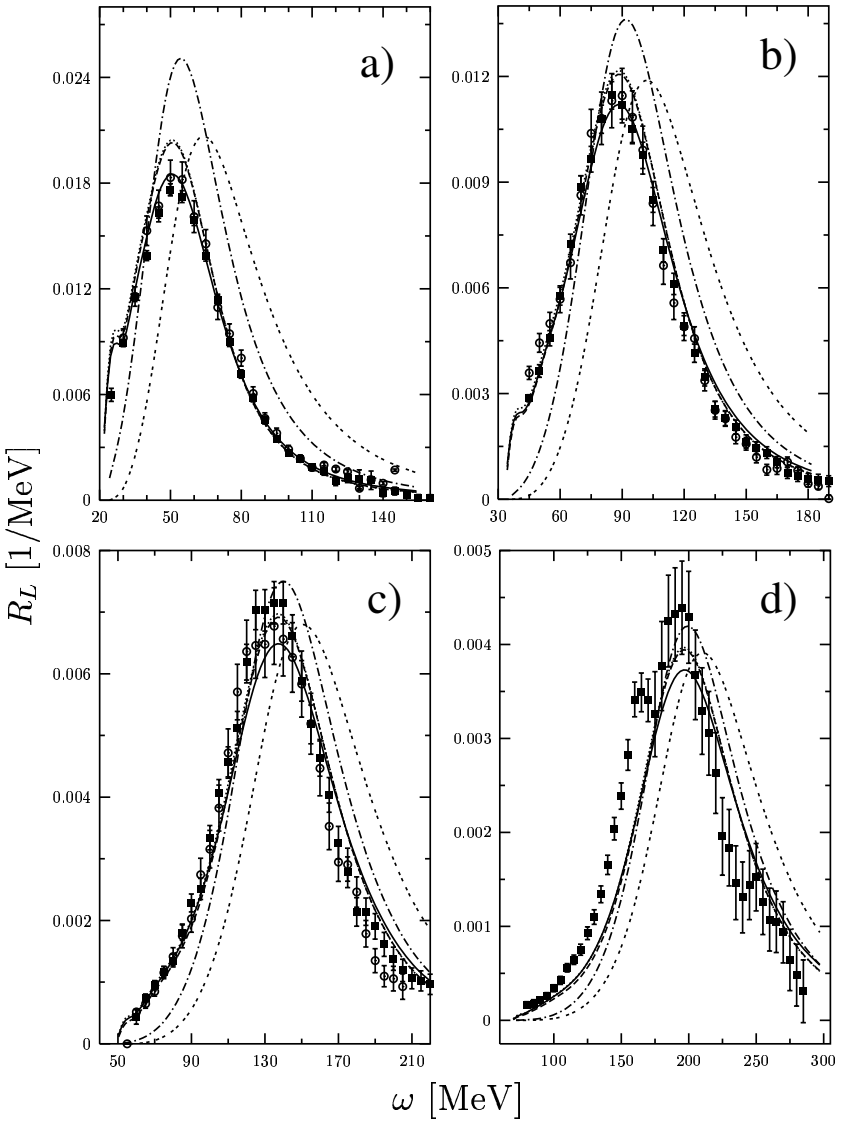

Fig. 5. The R_L response function against the energy transfer ω for $Q = 300$ (a), 400 (b), 500 (c), and 600 MeV/c (d). The curves describe results based on the approximate treatment of FSI (called FSI23 in the text) (dash-dotted line), the results under full inclusion of FSI but without MEC (dotted line), the full calculations including MEC (dashed line) and the full calculations which incorporate both π- and ρ-like MEC [10] and 3N force (here Urbana IX [14]) effects (solid line). AV18 [9] is used as the NN potential. The double-dashed line corresponds to the pure (non-symmetrized) plane-wave results. The data are from [19] (squares) and from [20] (open circles). The FSI and FSI + MEC curves essentially overlap.

for the additional action of the two-body density operator, and, finally, on top of that, we see the action of a 3NF. From the figure it is clear that PWIA and FSI23 are rather inaccurate approximations to the full dynamics. FSI is extremely important but still misses the data. The contribution of the two-body density is marginal, but the action of the 3NF is quite substantial and leads to a nice agreement with the data at $Q = 300$ and 400 MeV/c. At the higher Q-values relativity is needed. We expect that relativistic kinematics will shift theory to the right position.

In the case of R_T an interesting interplay between MEC and 3NF effects occurs. While MEC effects shift the FSI results upwards in the peak region, additional 3NF effects shift them down again. Unfortunately the two available data sets at $Q = 300$ MeV/c are controversial and do not allow to decide about agreement or disagreement between the theory and the data. In view of that interesting interplay precise new data in the peak region would be very desirable. On the theory side, it would be interesting to investigate the role of possible 3N currents related to the 3NF used. Also here relativistic kinematics are required, at least at the two higher Q-values.

The two response functions going with the helicity of the polarized electron beam (occurring in eq. (17)) are equally sensitive to FSI, MEC and 3NF effects and are displayed in figs. 7 and 8. While for $\tilde{R}_{T'}$ MEC and 3NF

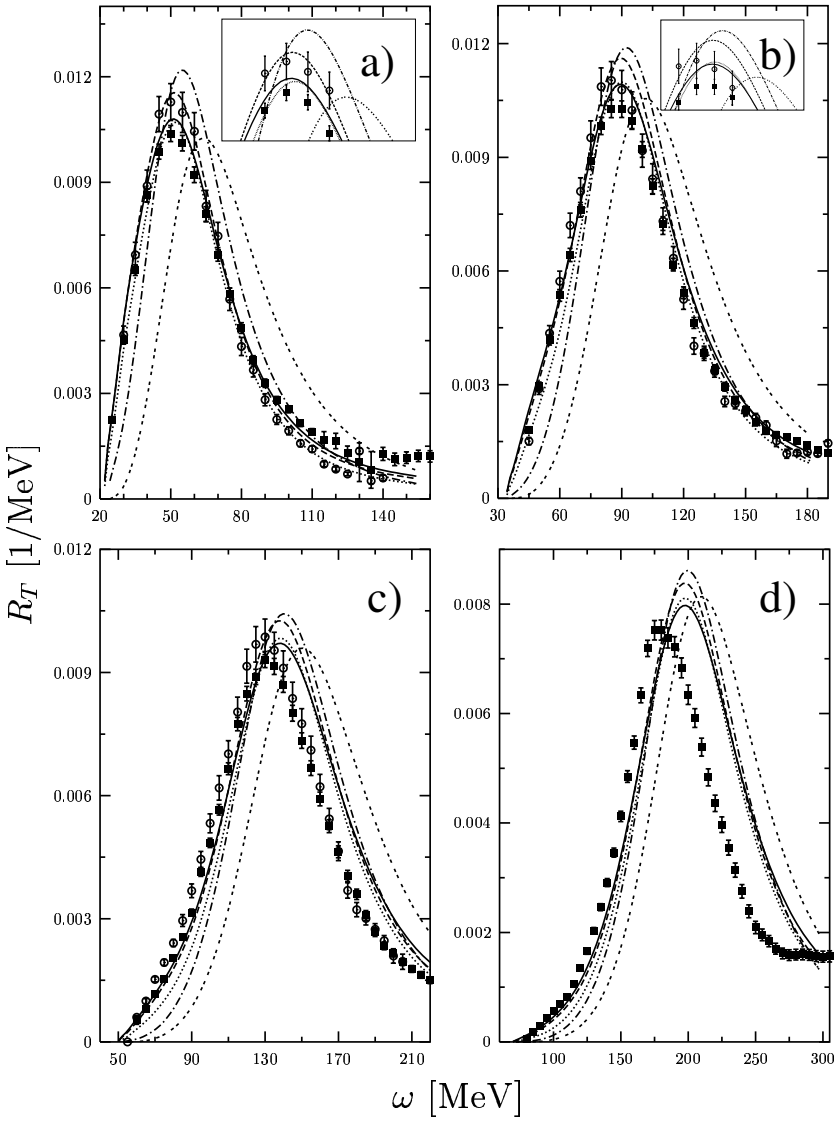

Fig. 6. The same as in fig. 5 for the R_T response function.

effects move the pure FSI result in the same direction, the opposite is true for $\tilde{R}_{TL'}$. In that latter response function the various effects are quite pronounced and one sees a strong ω-dependent structure. Therefore, data would be extremely valuable to test all the dynamical ingredients.

Some experimental information is, however, already available in form of asymmetries

$$A \equiv \frac{\frac{\mathrm{d}^3\sigma}{\mathrm{d}\Omega_{\mathrm{e}'}\mathrm{d}E'}\Big|_{h=+1} - \frac{\mathrm{d}^3\sigma}{\mathrm{d}\Omega_{\mathrm{e}'}\mathrm{d}E'}\Big|_{h=-1}}{\frac{\mathrm{d}^3\sigma}{\mathrm{d}\Omega_{\mathrm{e}'}\mathrm{d}E'}\Big|_{h=+1} + \frac{\mathrm{d}^3\sigma}{\mathrm{d}\Omega_{\mathrm{e}'}\mathrm{d}E'}\Big|_{h=-1}}$$
$$= -\frac{v_{T'}\tilde{R}_{T'}\cos\theta^* + v_{TL'}\tilde{R}_{TL'}2\sin\theta^*\cos\phi^*}{v_L R_L + v_T R_T}. \qquad (17)$$

This well-known expression shows the explicit θ^* and ϕ^* dependence of A. In fig. 9 we display the theoretical results for A together with the data [21] taken around $\theta^* = 0°$. This allowed us to extract the magnetic neutron form factor at two q^2-values, 0.1 and 0.2 $(\mathrm{GeV}/c)^2$ [21]. The well-known property, $\tilde{R}_{T'} \propto (G_M^{\mathrm{n}})^2$, valid in PWIA [13] (and references therein), is lost if the full dynamics are acting, nevertheless sufficient sensitivity to G_M^{n} survives. The results for G_M^{n} extracted from ^{3}He agree perfectly well with the values extracted from the deuteron [22] (see fig. 10).

At the higher q^2-values also measured in [21], our dynamical ingredients failed, which points to relativistic effects in kinematics and dynamics. In a subsequent experiment [23] the relation (17) has been checked around $\theta^* = 135°$, where both response functions contribute. The result is quite satisfying as shown in one example in fig. 11. Nevertheless a systematic experimental study of $\tilde{R}_{T'}$ and $\tilde{R}_{TL'}$ is very much needed because their richer structure will be

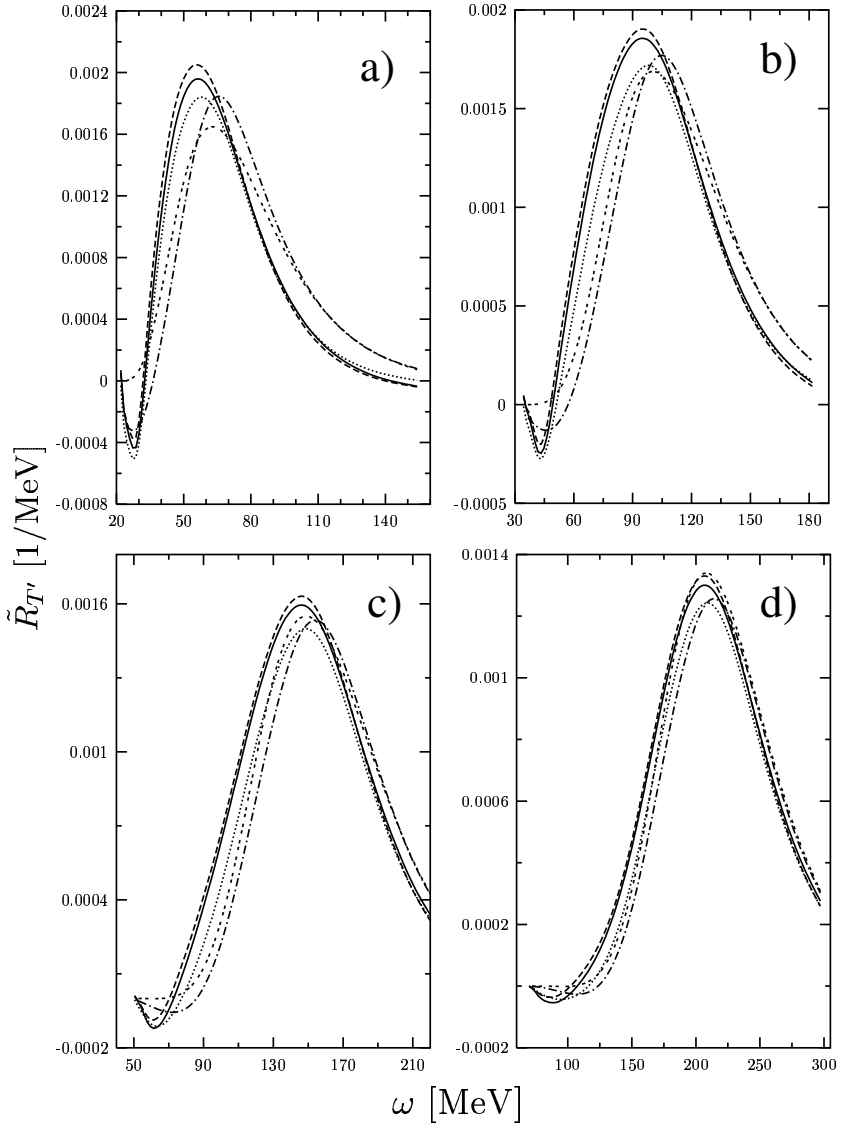

Fig. 7. The same as in fig. 5 for the $\tilde{R}_{T'}$ response function.

much more helpful for the detailed test of all aspects of the dynamics than the asymmetries measured so far.

3.3 The pd breakup of ^{3}He

The pd breakup process shows two prominent structures, the proton and deuteron knockout peaks. It is well known that in PWIA the process in parallel kinematics shown in fig. 12 leads to a peak in the angular distribution of the proton, while the two processes shown in fig. 13 lead to a peak in the angular distribution of the deuteron. The three diagrams together correspond to taking a fully antisymmetrized final state, which is denoted by PWIAS. The diagram in fig. 12 and the two in fig. 13 contribute selectively either to one or to the other peak. It is of interest to investigate rescattering processes for both peaks. This is displayed in two kinematical examples in figs. 14 and 15.

For $Q = 250$ MeV/c we see in PWIA just the p-knockout peak around $\theta_{\rm p} = 60°$. PWIAS shows an additional peak around $\theta_{\rm p} = 240°$ but its two additional (beyond PWIA) diagrams do not contribute around 60°. Conversely PWIA does not contribute around $\theta_{\rm p} = 240°$. That additional peak, the deuteron peak, is clearly visible when plotted against the deuteron scattering angle $\theta_{\rm d}$. For the Q-value of fig. 14 FSI effects are strongly visible in both peaks and also MEC effects to some extent. This is different at $Q = 431$ MeV/c (see fig. 15), where only the deuteron peak is strongly affected by FSI, whereas the p-peak can be described quite well by the most simple process, PWIA. For that Q-value MEC effects are nearly negligible.

It would be very desirable to measure both peak regions in one and the same experiment (the same virtual photon). To the best of our knowledge the two regions have only been investigated in separate experiments. We show

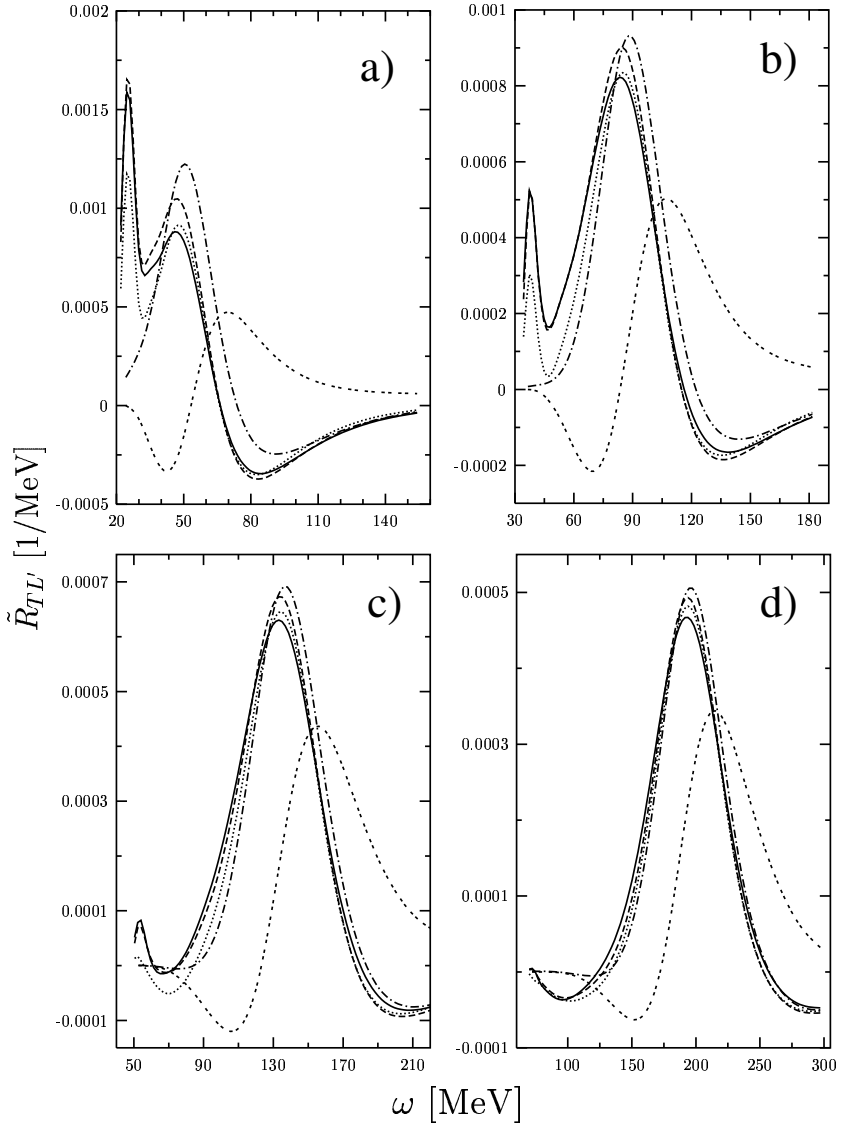

Fig. 8. The same as in fig. 5 for the $\tilde{R}_{TL'}$ response function.

one example in fig. 16. Even for p-knockout only a part of the peak region has been covered by the data. Precise data covering the whole region would be desirable at low and somewhat higher Q-values. At least at the higher Q-values theoretical predictions should be correct since the simple diagram in PWIA is just an overlap of the deuteron and the ^{3}He state at relatively low deuteron momenta. At the low Q-values FSI will play a role but the nuclear forces used describe pd scattering quite well and MEC effects are very small. Therefore also in this case agreement to the data should be expected. These expectations should be verified by comparison to data.

The situation is even more interesting in the d-peak, shown in fig. 17, where theory fails dramatically. Further precise data would be very valuable to solidify that failure. A confirmation would call for an improvement in the currents. Also the role of the 3N forces in the continuum has to be further studied.

3.4 The full breakup of ^{3}He

In case of the complete-breakup ^{3}He(e, e′pp) and ^{3}He(e, e′pn) we refer to [24] and [25]. Unfortunately these data were taken in a kinematical regime where the 3N c.m. energy is above the pion threshold and serious discrepancies showed up in the comparison to the (inadequate) theory. Data at lower energy transfers would very likely provide interesting insight into the interplay of NN forces, 3N forces and MECs, similar to what we found in photon-induced breakup processes [5,26]. Here we display two kinematically complete electron-induced breakup cross-sections with interesting pronounced structures. The strong peaks in fig. 18 arise since around $S = 8$ MeV and 30 MeV (arc length along the kinematical locus) two nucleons leave with equal momentum vectors. For $S \approx 8$ MeV this happens in the neutron-proton (23) subsystem and for $S \approx 30$ MeV in the proton-proton subsystem (13).

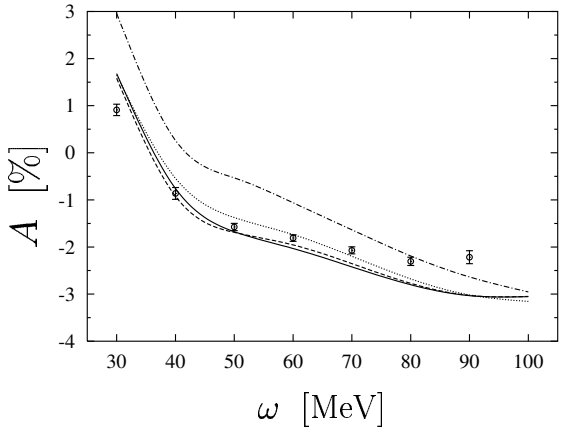

Fig. 9. The asymmetry A of eq. (17) together with data from [21] for $q^2 = 0.1$ (GeV/c)^2 around $\theta^* = 0^\circ$. Curves as in fig. 5.

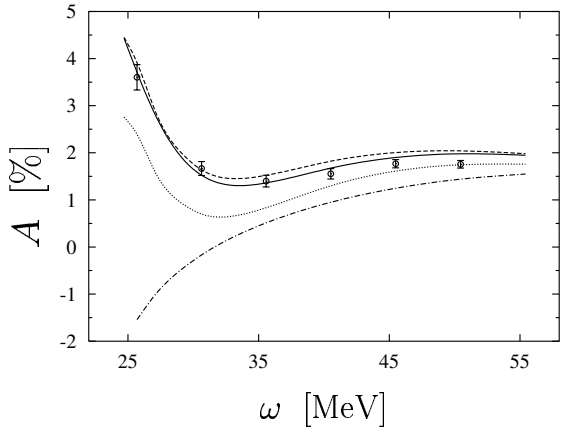

Fig. 11. The asymmetry A at $q^2 = 0.1$ (GeV/c)^2 around $\theta^* = 135^\circ$. The curves as in fig. 9 are shown together with data from [23].

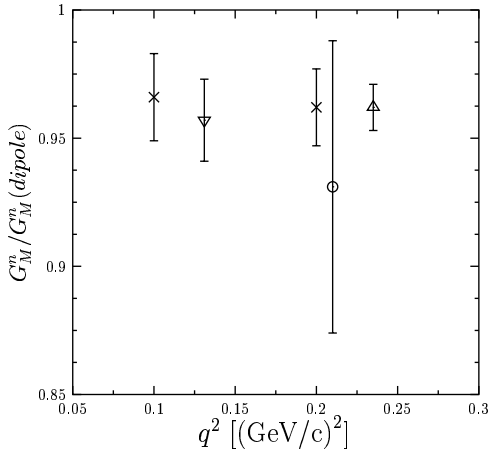

Fig. 10. G_M^n-values extracted from different measurements on the deuteron ([27] ($\bigtriangledown$), [28] ($\bigtriangleup$)) and on ^{3}He ([29] ($\bigcirc$), [21] ($\times$)). For the sake of visibility the two deuteron results ($\bigtriangledown$ and $\bigtriangleup$) are shifted sidewards but belong to $q^2 = 0.1$ and 0.2 (GeV/c)^2, respectively.

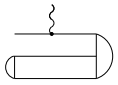

Fig. 12. The diagram corresponding to PWIA.

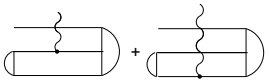

Fig. 13. The diagrams corresponding to the rest of PWIAS.

Of course, these peak structures are entirely the result of FSI. The peaks in fig. 19 shown against the scattering angle of a nucleon in relation to the virtual-photon direction correspond to a coplanar "Mercedes star" configuration, where the three final nucleons have equal energies and leave under 120° pairwise angles. This is reflected in the repetition of the peaks in steps of 120°. Interestingly, also in this configuration, FSIs are clearly an important aspect of the dynamics of the reaction.

3.5 Semi-exclusive nucleon knockout processes

Finally, we regard the ^{3}He(e, e′p)pn and ^{3}He(e, e′n)pp semi-exclusive processes. In parallel kinematics and under quasi-free scattering conditions the spectral function has been an often used tool to analyze the data [30]. It is based on the simple picture that the photon is absorbed by the knocked-out nucleon which leaves without any interaction. Only the two spectator nucleons interact with each other via the NN t-operator. This picture corresponds to the two framed diagrams in fig. 1. In a forthcoming paper [31] we shall investigate in some detail the limitations of that picture in the kinematical region considered in this paper and display here only some examples. It is easily seen under the simplifying assumption of the two diagrams that the spectral function is related to the response functions R_L and R_T as

$$S(E,k) = \frac{1}{2}\, m\, p_{23}\, \frac{1}{(G_E)^2} \int \mathrm{d}\hat{p}_{23} R_L(\mathrm{FSI23}) = \frac{1}{2}\, m\, p_{23}\, \frac{2m^2}{Q^2 (G_M)^2} \int \mathrm{d}\hat{p}_{23} R_T(\mathrm{FSI23}). \quad (18)$$

The index FSI23 stands for FSI acting only in the pair 23 when nucleon 1 absorbs the photon. G_E and G_M are the electric and magnetic nucleon form factors and p_{23} the relative momentum of the spectator nucleons 2 and 3. These expressions can now be compared to the following

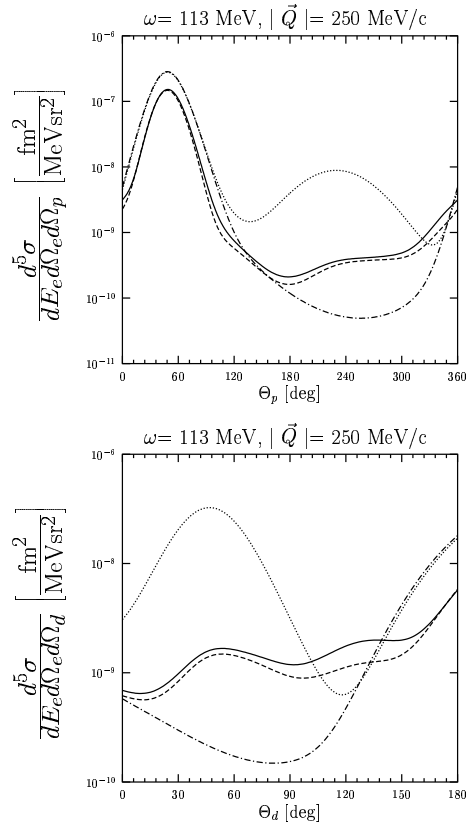

Fig. 14. The proton (top) and deuteron (bottom) angular distributions for the two-body breakup of ^{3}He. The curves depict PWIA (dash-dotted line) and PWIAS (dotted line) results, the full calculations without MEC (dashed line) and the full calculations which incorporate both π- and ρ-like MEC (solid line). AV18 is used as the NN potential.

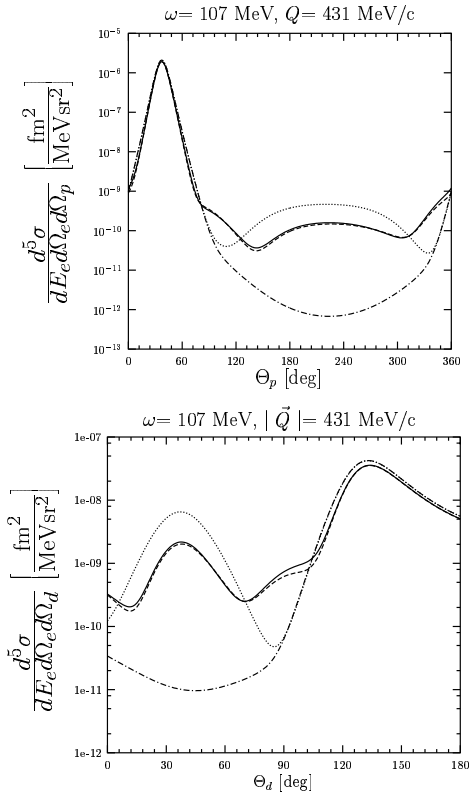

Fig. 15. The same as in fig. 14 but for a different (ω, Q) pair.

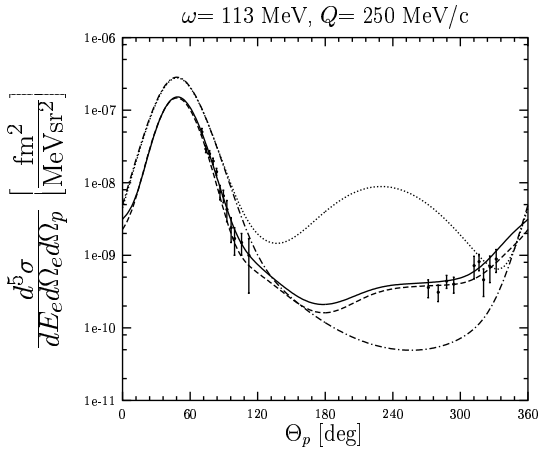

Fig. 16. The whole proton angular distribution in the same kinematics as chosen in fig. 14. The data are from [32]. The curves are as in fig. 14.

expressions:

$$
\begin{aligned}
S(E,k)_L^{\mathrm{FSI}} &= \frac{1}{2}\, m\, p_{23}\, \frac{1}{(G_E)^2} \int \mathrm{d}\hat{p}_{23} R_L(\mathrm{FSI}),\\
S(E,k)_T^{\mathrm{FSI}} &= \frac{1}{2}\, m\, p_{23}\, \frac{2m^2}{Q^2(G_M)^2} \int \mathrm{d}\hat{p}_{23} R_T(\mathrm{FSI}),\\
S(E,k)_L^{\mathrm{PWIA}} &= \frac{1}{2}\, m\, p_{23}\, \frac{1}{(G_E)^2} \int \mathrm{d}\hat{p}_{23} R_L(\mathrm{PWIA}),\\
S(E,k)_T^{\mathrm{PWIA}} &= \frac{1}{2}\, m\, p_{23}\, \frac{2m^2}{Q^2(G_M)^2} \int \mathrm{d}\hat{p}_{23} R_T(\mathrm{PWIA}),\\
S(E,k)_L^{\mathrm{PWIAS}} &= \frac{1}{2}\, m\, p_{23}\, \frac{1}{(G_E)^2} \int \mathrm{d}\hat{p}_{23} R_L(\mathrm{PWIAS}),\\
S(E,k)_T^{\mathrm{PWIAS}} &= \frac{1}{2}\, m\, p_{23}\, \frac{2m^2}{Q^2(G_M)^2} \int \mathrm{d}\hat{p}_{23} R_T(\mathrm{PWIAS}),
\end{aligned}
\tag{19}
$$

where $R_{L,T}$(FSI), $R_{L,T}$(PWIA) and $R_{L,T}$(PWIAS) are the response functions calculated with the complete FSI, just using PWIA or finally the symmetrized version PWIAS. For various fixed (ω, Q) pairs we show in figs. 20-23 the quantities $S(E,k)$ as a function of E_1, the energy of the knocked-out nucleon. To each E_1 corresponds uniquely the value of the missing momentum k ($\vec{k} = \vec{p}_1 - \vec{Q}$) and excitation energy $E = p_{23}^2/m$. We display in table 1 the kinematical variables underlying figs. 20-23. This together with the $S(E,k)$ given in figs. 20-23 is a substitute for plotting $S(E,k)$ over the (E,k)-plane.

Let us first regard the p-knockout in figs. 20 and 21. For R_L only in case of $Q = 600$ MeV/c the use of the

Table 1. The relation between E_1, the energy of the nucleon ejected parallel to $\vec{Q}$, and $(E,\, k)$, the arguments of the spectral function $S(E,k)$ for four different values of Q. In all cases the energy transfer $\omega = 150$ MeV.

E_1 (MeV)	E (MeV)	k (fm^{-1})
	$Q = 200$ MeV/c	
50.0	89.27	0.54
70.0	65.24	0.82
90.0	40.41	1.07
110.0	15.04	1.29
121.7	0.00	1.41
	$Q = 300$ MeV/c	
60.0	81.94	0.18
80.0	60.24	0.44
100.0	37.55	0.68
120.0	14.15	0.89
131.9	0.00	1.00
	$Q = 400$ MeV/c	
50.0	89.95	0.47
60.0	81.18	0.33
80.0	62.24	0.06
100.0	41.99	0.17
120.0	20.80	0.38
139.0	0.00	0.56
	$Q = 600$ MeV/c	
50.0	69.34	1.49
70.0	57.28	1.20
90.0	42.78	0.96
110.0	26.65	0.74
130.0	9.30	0.54
140.3	0.00	0.44

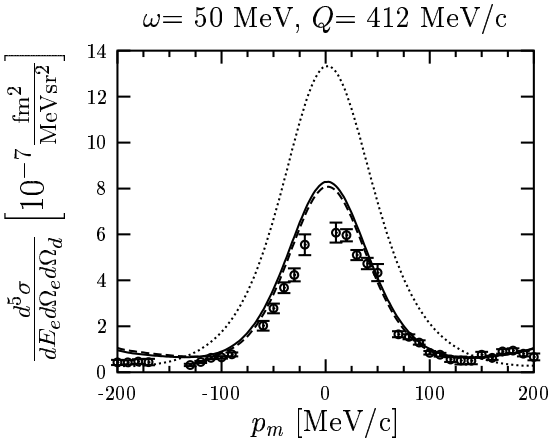

Fig. 17. The deuteron knockout peak area as a function of the missing (*i.e.* proton) momentum. The data are from [33]. The curves are as in fig. 14 except that the PWIA prediction (totally negligible) is not shown.

spectral function S is a good approximation at the upper end of E_1, where the FSI (solid line) and FSI23 (dotted line) predictions coincide. For that restricted energy range in E_1 the absorption of the photon by nucleons 2 and 3, as

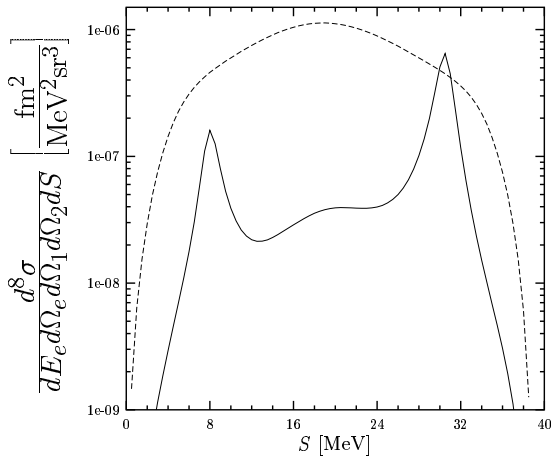

Fig. 18. The cross-section for the three-body breakup of ^{3}He for fixed angles of two outgoing nucleons as a function of the arc length S. The PWIAS (dashed line) and full results without MEC and 3NF (solid line) are shown. The incoming-electron energy $E_e = 390$ MeV, $\omega = 37$ MeV and $Q = 100$ MeV/c are chosen. The proton angles are $\theta_1 = 11^\circ$ and $\phi_1 = 0^\circ$, while the second observed nucleon (neutron) is emitted with $\theta_2 = 139^\circ$ and $\phi_1 = 180^\circ$.

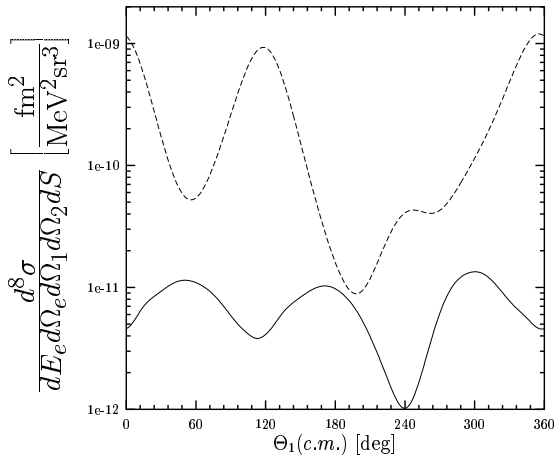

Fig. 19. The cross-section for the three-body breakup of ^{3}He in the so-called "plane star" configuration as a function of the c.m. angle of the ejected proton. The PWIAS (dashed line) and full results without MEC and 3NF (solid line) are shown. The incoming-electron energy $E_e = 390$ MeV, $\omega = 113$ MeV and $Q = 250$ MeV/c are chosen.

added in for PWIAS, provides a negligible contribution to the PWIA result. This is of course different at smaller E_1-values (not shown). The approximate use of S in case of R_T shown in fig. 21 is more justified. In all cases PWIA or PWIAS would be meaningless.

In case of n-knockout shown in figs. 22 and 23 FSI is much more present for R_L than for p-knockout. Here the use of the spectral function would be quite erroneous. In case of R_T, however, the situation is similar as for p-knockout. Now the results for PWIA and PWIAS differ, which is due to the strong absorption on the proton.

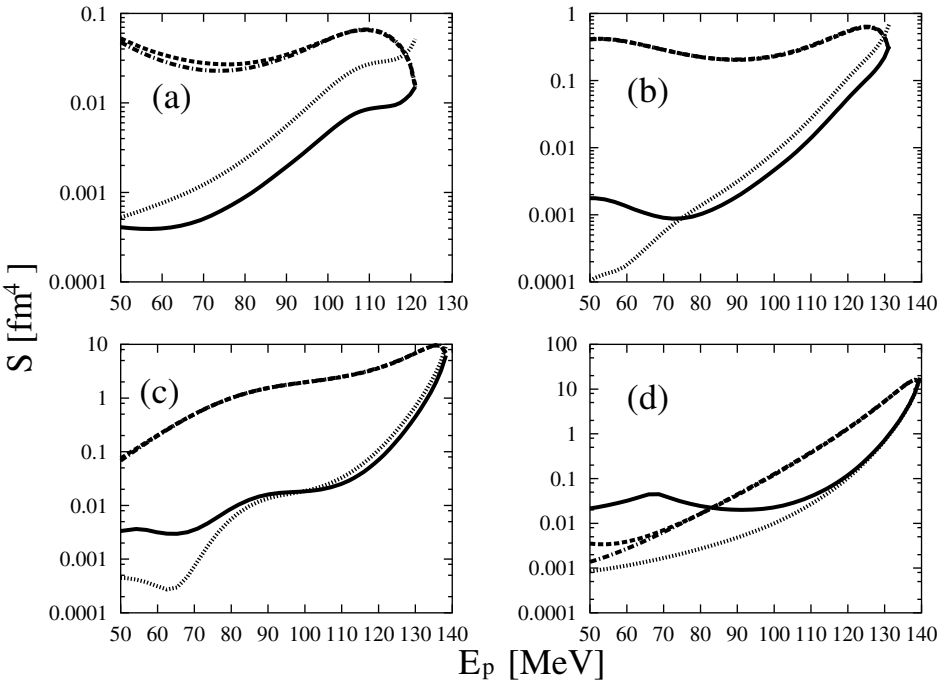

Fig. 20. The proton spectral function $S(E,k)$ and related S-functions from eq. (19) extracted from R_L for parallel kinematics at $\omega = 150$ MeV and four different Q-values: $Q = 200$ MeV/c (a), $Q = 300$ MeV/c (b), $Q = 400$ MeV/c (c) and $Q = 600$ MeV/c (d). The PWIA (dash-dotted line), FSI23 (dotted line), PWIAS (dashed line) and full results (solid line) are shown as a function of the ejected proton energy. The FSI23 result is just the spectral function S from eq. (18).

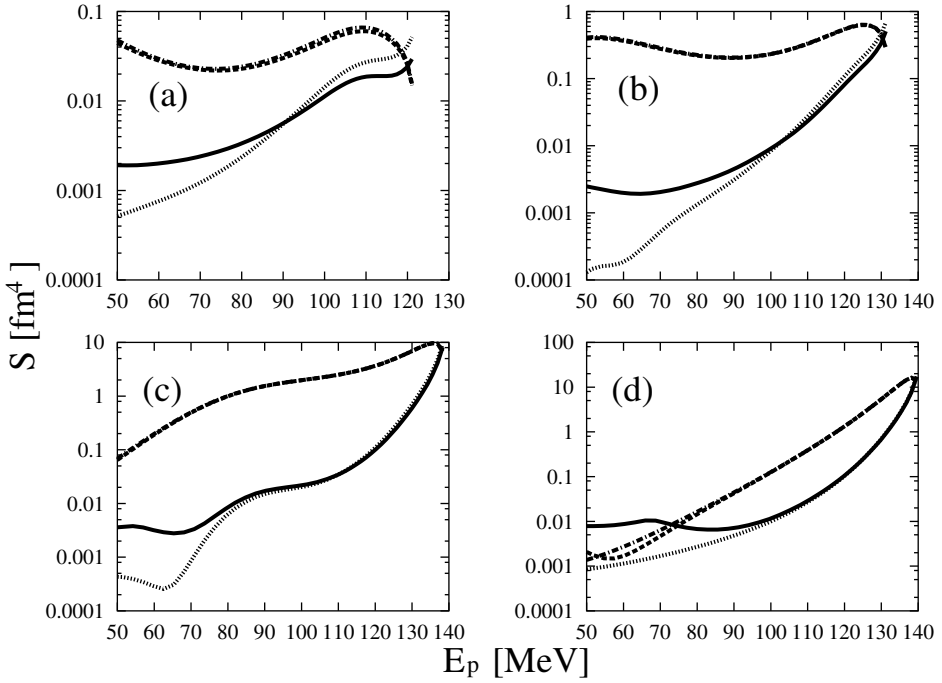

Fig. 21. The proton spectral function $S(E,k)$ and related S-functions from eq. (19) extracted from R_T for the same conditions as in fig. 20.

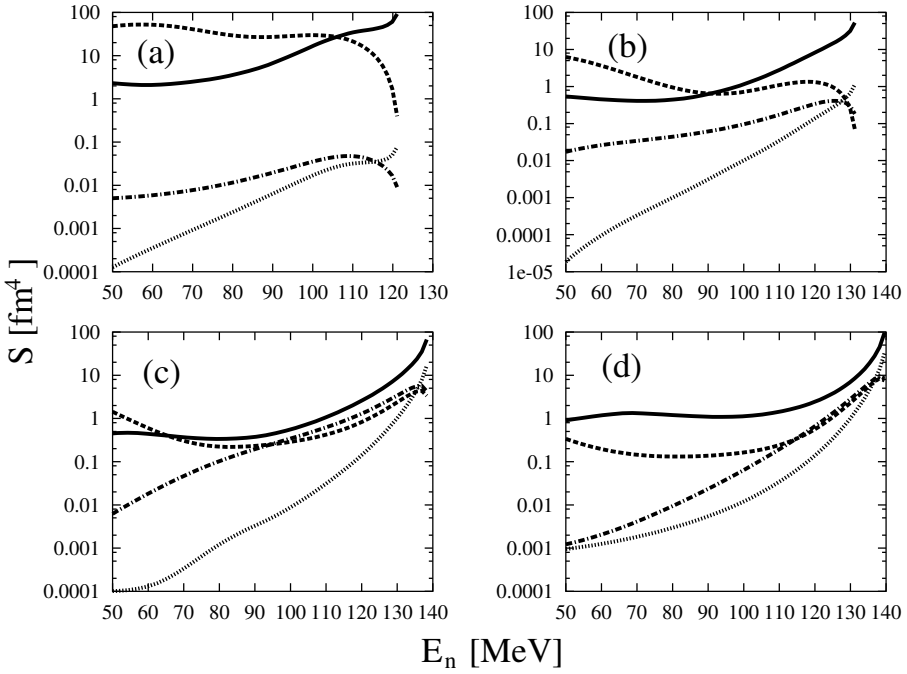

Fig. 22. The neutron spectral function $S(E,k)$ and related S-functions from eq. (19) extracted from R_L for the same conditions as in fig. 20.

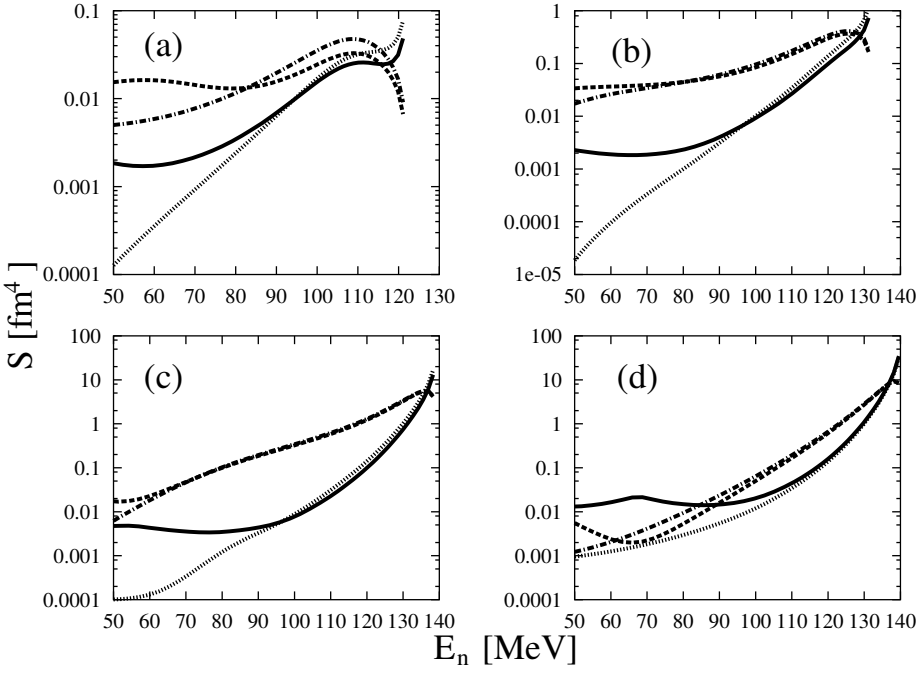

Fig. 23. The neutron spectral function $S(E,k)$ and related S-functions from eq. (19) extracted from R_T for the same conditions as in fig. 20.

Systematic measurements related to those examples would be very helpful to test the dynamics.

This would be especially gratifying in case of the neutron knockout which should be well understood in order to extract the electric form factor of the neutron in a reliable manner. We refer to [34] where the process $\overrightarrow{^3\mathrm{He}}(\vec{e}, e'n)$ has been studied extensively with the result that for the kinematical region considered here FSI is extremely important. Outside the $(\omega - Q)$ domain considered here the use of $S(E, k)$ might be more favorable [30] but its justification requires a relativistic treatment.

4 Outlook

We showed for various observables in electron-induced inelastic processes on ^{3}He that they challenge our present-day understanding of nuclear forces and currents. The 3N system is an ideal laboratory since all reactions can be safely calculated in the Faddeev scheme and no uncontrolled approximations blur the comparison between theory and experiment. There are quite a few discrepancies using the modern NN forces and the still too restricted set of 3N forces and exchange currents. For more examples we refer to [21,33,25,35–37]. Dedicated and precise experiments, some of which are pointed out, would certainly help to lay a solid ground of data, which present and future theory have to describe.

One can expect that the theoretical approach via effective field theory constrained by chiral symmetry will lay a corresponding sound basis in theory, since NN and 3N forces as well as exchange currents follow from one and the same underlying Lagrangian and are therefore consistently defined. This upcoming theoretical formulation will call even more for adequate data in the energy regime considered here.

This work was supported by the Polish Committee for Scientific Research under grant No. 2P03B00825, by the NATO grant No. PST.CLG.978943 and by DOE under grants Nos. DE-FG03-00ER41132 and DE-FC02-01ER41187. The numerical calculations have been performed on the Cray SV1 and T3E of the NIC in Jülich, Germany. R.S. thanks the Foundation for Polish Science for financial support.

References

1. H. Witała *et al.*, Phys. Rev. C **63**, 024007 (2001); J. Kuroś-Żołnierczuk *et al.*, Phys. Rev. C **66**, 024003 (2002).
2. K. Sekiguchi *et al.*, Phys. Rev C **65**, 034003 (2002); E. Ermisch *et al.*, submitted to Phys. Rev. C, nucl-ex/0308012; K. Sekiguchi *et al.*, to be published in Phys. Rev. C.
3. A. Nogga *et al.*, Phys. Rev. C **67**, 034004 (2003).
4. W. Glöckle, *The Quantum Mechanical Few-Body Problem* (Springer-Verlag, Berlin, 1983).
5. R. Skibiński *et al.*, Phys. Rev. C **67**, 054001 (2003).
6. H. Witała *et al.*, Few-Body Syst. **3**, 123 (1988).
7. J. Golak *et al.*, Phys. Rev. C **51**, 1638 (1995).
8. J. Golak *et al.*, Phys. Rev. C **52**, 1216 (1995).
9. R.B. Wiringa *et al.*, Phys. Rev. C **51**, 38 (1995).
10. D.O. Riska, Phys. Scr. **31**, 107; 471 (1985).
11. J. Carlson, R. Schiavilla, Rev. Mod. Phys. **70**, 743 (1998).
12. R. Schiavilla *et al.*, Phys. Rev. C **41**, 309 (1990).
13. S. Ishikawa *et al.*, Phys. Rev. C **57**, 39 (1998); J. Golak *et al.*, Phys. Rev. C **63**, 034006 (2001)
14. B.S. Pudliner *et al.*, Phys. Rev. C **56**, 1720 (1997).
15. T.W. Donnelly, A.S. Raskin, Ann. Phys. (N.Y.) **169**, 247 (1986).
16. A.S. Raskin, T.W. Donnelly, Ann. Phys. (N.Y.) **191**, 78 (1989).
17. W. Glöckle *et al.*, in *Proceedings of the Second Workshop on Electronuclear Physics with Internal Targets and the BLAST detector*, edited by R. Alarcon, R. Milner (World Scientific, 1999) pp. 185-207.
18. A. Amroun *et al.*, Nucl. Phys. A **579**, 596 (1994) and references therein; I. Sick, private communication.
19. C. Marchand *et al.*, Phys. Lett B **153**, 29 (1995).
20. K. Dow *et al.*, Phys. Rev. Lett. **61**, 1706 (1988).
21. W. Xu *et al.*, Phys. Rev. Lett. **85**, 2900 (2000).
22. H. Anklin *et al.*, Phys. Lett. B **428**, 248 (1998).
23. F. Xiong *et al.*, Phys. Rev. Lett. **87**, 242501 (2001).
24. D.L. Groep *et al.*, Phys. Rev. Lett. **83**, 5443 (1999).
25. D.L. Groep *et al.*, Phys. Rev. C **63**, 014005 (2001).
26. R. Skibiński *et al.*, Phys. Rev. C **67**, 054002 (2003).
27. H. Anklin *et al.*, Phys. Lett. B **336**, 313 (1994)
28. H. Anklin *et al.*, Phys. Lett. B **428**, 248 (1998).
29. H. Gao *et al.*, Phys. Rev. C **50**, R546 (1994); Nucl. Phys. A **631**, 170c (1998).
30. C. Ciofi degli Atti, L.P. Kaptari, Phys. Rev. C **66**, 044004 (2002) and references therein.
31. J. Golak *et al.*, to be published in Phys. Rev. C.
32. P.H.M. Keizer, PhD Thesis, Amsterdam, 1986; E. Jans, private communication.
33. C.M. Spaltro *et al.*, Nucl. Phys. A **706**, 403 (2002).
34. J. Golak *et al.*, Phys. Rev. C **65**, 044002 (2002); **66**, 024008 (2002).
35. R.S. Hicks *et al.*, Phys. Rev. C **67**, 064004 (2003).
36. C.M. Spaltro *et al.*, Phys. Rev. Lett. **81**, 2870 (1998).
37. S. Ishikawa *et al.*, Nuovo Cimento A **107**, 305 (1994).